

Dual roles of oxygen-annealing in modulating the superconductivity of $La_3Ni_2O_{7+\delta}$

Xin-Ran Hu(胡欣然), Jia Yu(于佳), Jun-Kun Yi(易俊锟), Ya-Dong Gu(谷亚东), Jun-Jie Feng(冯俊杰), Xie-Yu Sun(孙谢羽), Qing-Song Liu(刘青松), Yun-Qing Shi(石运清), Meng-Hu Zhou(周孟虎), Hui-Ran Sun(孙慧冉), Chang-Sheng Jiang(蒋长胜), Qi-Heng Huang(黄启衡), Tao Han(韩涛), Ming-Sheng Long(龙明生), Xing-Yuan Hou(侯兴元), Bing-Hui Ge(葛炳辉), Dong-Sheng Song(宋东升), Zhi-An Ren(任治安), Qing-Ge Mu(穆青隔), and Lei Shan(单磊)

Citation: Chin. Phys. B, 2026, 35 (**5**): 057407. DOI: 10.1088/1674-1056/ae5050
http://cpb.iphy.ac.cn; http://iopscience.iop.org/cpb

What follows is a list of articles you may be interested in

Structure and superconducting properties of $Ru_{1-x}Mo_x$ (x = 0.1—0.9) alloys

Yang Fu(付阳), Chunsheng Gong(龚春生), Zhijun Tu(涂志俊), Shangjie Tian(田尚杰), Shouguo Wang(王守国), and Hechang Lei(雷和畅)

Chin. Phys. B, 2024, 33 (**4**): 047404. DOI: 10.1088/1674-1056/ad2a73

Thermal conductivity of GeTe crystals based on machine learning potentials

Jian Zhang(张健), Hao-Chun Zhang(张昊春), Weifeng Li(李伟峰), and Gang Zhang(张刚)

Chin. Phys. B, 2024, 33 (**4**): 047402. DOI: 10.1088/1674-1056/ad1b42

A ten-fold coordinated high-pressure structure in hafnium dihydrogen with increasing superconducting transition temperature induced by enhancive pressure

Yan-Qi Wang(王妍琪), Chuan-Zhao Zhang(张传钊), Jin-Quan Zhang(张金权), Song Li(李松), Meng Ju(巨濛), Wei-Guo Sun(孙伟国), Xi-Long Dou(豆喜龙), and Yuan-Yuan Jin(金园园)

Chin. Phys. B, 2023, 32 (**9**): 097402. DOI: 10.1088/1674-1056/acc934

Conservation of the particle-hole symmetry in the pseudogap state in optimally-doped $Bi_2Sr_2CuO_{6+\delta}$ superconductor

Hongtao Yan(闫宏涛), Qiang Gao(高强), Chunyao Song(宋春尧), Chaohui Yin(殷超辉), Yiwen Chen(陈逸雯), Fengfeng Zhang(张丰丰), Feng Yang(杨峰), Shenjin Zhang(张申金), Qinjun Peng(彭钦军), Guodong Liu(刘国东), Lin Zhao(赵林), Zuyan Xu(许祖彦), and X. J. Zhou(周兴江)

Chin. Phys. B, 2022, 31 (**8**): 087401. DOI: 10.1088/1674-1056/ac7214

Doping effects of transition metals on the superconductivity of (Li,Fe)OHFeSe films

Dong Li(李栋), Peipei Shen(沈沛沛), Sheng Ma(马晟), Zhongxu Wei(魏忠旭), Jie Yuan(袁洁), Kui Jin(金魁), Li Yu(俞理), Fang Zhou(周放), Xiaoli Dong(董晓莉), and Zhongxian Zhao(赵忠贤)

Chin. Phys. B, 2021, 30 (**1**): 017402. DOI: 10.1088/1674-1056/abd2ab

---

SPECIAL TOPIC — Superconductivity in nickel oxides

Dual roles of oxygen-annealing in modulating the superconductivity of $La_3Ni_2O_{7+\delta}$

Xin-Ran Hu(胡欣然)[1,2,†], Jia Yu(于佳)[3,†], Jun-Kun Yi(易俊锟)[4,5,†], Ya-Dong Gu(谷亚东)[4,5], Jun-Jie Feng(冯俊杰)[1,2], Xie-Yu Sun(孙谢羽)[1,2], Qing-Song Liu(刘青松)[4,5], Yun-Qing Shi(石运清)[4,5], Meng-Hu Zhou(周孟虎)[4,5,6], Hui-Ran Sun(孙慧冉)[1,2], Chang-Sheng Jiang(蒋长胜)[1,2], Qi-Heng Huang(黄启衡)[1,2], Tao Han(韩涛)[1,2], Ming-Sheng Long(龙明生)[1,2], Xing-Yuan Hou(侯兴元)[1,2], Bing-Hui Ge(葛炳辉)[1], Dong-Sheng Song(宋东升)[1,¶], Zhi-An Ren(任治安)[4,5], Qing-Ge Mu(穆青隔)[1,2,7,§], and Lei Shan(单磊)[1,2,8,‡]

[1] *Information Materials and Intelligent Sensing Laboratory of Anhui Province, Institutes of Physical Science and Information Technology, Anhui University, Hefei* 230601, *China*

[2] *Leibniz International Joint Research Center of Materials Sciences of Anhui Province, Center of Free Electron Laser & Strong Magnetic Field, State Key Laboratory of Opto-Electronic Information Acquisition and Protection Technology, Anhui University, Hefei* 230601, *China*

[3] *Quantum Science Center of Guangdong–Hong Kong–Macao Greater Bay Area (Guangdong), Shenzhen* 518000, *China*

[4] *Institute of Physics and Beijing National Laboratory for Condensed Matter Physics, Chinese Academy of Sciences, Beijing* 100190, *China*

[5] *School of Physical Sciences, University of Chinese Academy of Sciences, Beijing* 100049, *China*

[6] *School of Science, Hunan Institute of Technology, Hengyang* 421002, *China*

[7] *Key Laboratory of Structure and Functional Regulation of Hybrid Materials (Anhui University), Ministry of Education, Hefei* 230601, *China*

[8] *Hefei National Laboratory, Hefei* 230088, *China*

(Received 7 January 2026; revised manuscript received 3 March 2026; accepted manuscript online 11 March 2026)

Oxygen deficiency is known to critically influence the superconductivity of $La_3Ni_2O_{7-\delta}$. However, precise control of oxygen content to mitigate such deficiencies remains a significant challenge. In this work, we synthesized high-oxygen-content $La_3Ni_2O_{7+\delta}$ polycrystals via high-pressure oxygen annealing with the oxygen stoichiometry (δ) successfully tuned by varying the amount of $KClO_4$. The obtained samples $La_3Ni_2O_{7.16}$ and $La_3Ni_2O_{7.38}$ exhibit metallic behavior at ambient pressure. We further conducted a comprehensive investigation into the pressure-induced superconductivity and atomic structure. STEM imaging revealed large-area bilayer-phase stacking in $La_3Ni_2O_{7.16}$, while $La_3Ni_2O_{7.38}$ showed noticeable intergrowth with other Ruddlesden–Popper (R–P) phases. Notably, the critical pressure in $La_3Ni_2O_{7.16}$ is substantially reduced, though its critical temperature (T_c) is lower than that of as-grown samples. In contrast, only a weak superconducting signal was detected in higher oxygen content sample $La_3Ni_2O_{7.38}$ likely due to the intergrowth with other R–P phases, non-negligible interstitial oxygen, or an increased fraction of the tetragonal phase. Our findings provide a viable pathway for optimizing nickelate superconductivity and offer insights into the fundamental mechanisms governing superconductivity in these materials.

Keywords: oxygen-annealing at high pressure, $La_3Ni_2O_7$, high temperature superconductivity, high pressure measurements

PACS: 74.62.–c, 74.62.Fj, 74.70.–b

DOI: 10.1088/1674-1056/ae5050 **CSTR:** 32038.14.CPB.ae5050

Since the discovery of high-temperature superconductivity (HTS) in cuprates, several new HTS materials have been identified over the past few decades.[1–5] Nevertheless, the fundamental mechanism underlying HTS remains unresolved. The development of novel HTS systems could provide crucial insights into this long-standing puzzle. Recently, the discovery of superconductivity in $La_3Ni_2O_{7-\delta}$ has generated significant interest, as this material exhibits a superconducting transition temperature (T_c) up to 80 K under moderate pressure.[6]

Extensive experimental and theoretical investigations have significantly advanced the understanding of nickelate superconductivity.[7–20] $La_3Ni_2O_7$ belongs to the Ruddlesden–Popper (R–P) family, with the general formula of $R_{n+1}Ni_nO_{3n+1}$, where R represents rare-earth elements, and n denotes the number of NiO_6 octahedra in the unit cell. Beyond the bilayer $La_3Ni_2O_{7-\delta}$, trilayer compounds $La_4Ni_3O_{10-\delta}$ and $Pr_4Ni_3O_{10-\delta}$ exhibit superconductivity with maximum T_c values up to 40 K,[21–23] while hybrid R–P phases (1212 and 1313 structures) have also been identified as superconductors.[24,25] Among these, the bilayer system demonstrates the highest T_c, reaching 96 K at optimal rare-earth doping levels.[26–31]

[†]These authors contributed equally to this work.

[‡]Corresponding author. E-mail: lshan@ahu.edu.cn

[§]Corresponding author. E-mail: mu@ahu.edu.cn

[¶]Corresponding author. E-mail: dsong@ahu.edu.cn

© 2026 Chinese Physical Society and IOP Publishing Ltd. All rights, including for text and data mining, AI training, and similar technologies, are reserved.

However, the superconductivity in $La_3Ni_2O_{7-\delta}$ displays strong sample dependence and pressure dependence.[19,32–37] Scanning transmission electron microscopy (STEM) studies reveal significant oxygen inhomogeneity, with vacancies primarily occupying inner apical sites, which may detrimentally affect superconductivity.[38] Theoretical analyses indicate that the Fermi pocket associated with $d_{3z^2-r^2}$ orbital plays a pivotal role in pressure-induced superconductivity, with strong interlayer coupling mediated by inner apical oxygen.[7,8,14,17,38] Oxygen deficiency at these sites disrupts interlayer electron hopping between Ni atoms and promotes the formation of local magnetic moments, both of which strongly suppress superconductivity.[7] These findings suggest that oxygen vacancy elimination could improve crystal quality and enhance superconducting properties.

Complementary studies on R–P phase nickelate thin films demonstrate the critical role of ozone oxidation in stabilizing superconductivity.[39–43] However, oxygen annealing of polycrystalline samples by high-oxygen-pressure method leads to bilayer structure degradation and weakened superconducting transitions.[44] Furthermore, high oxygen pressure induces interstitial oxygen formation, which also significantly suppresses superconductivity.[45,46] Consequently, systematic optimization of oxygen annealing parameters is crucial for both enhancing sample quality and uncovering the fundamental relationship between oxygen stoichiometry and superconductivity.

In this study, we performed high-pressure oxygen annealing at 2 GPa using a piston-cylinder-type apparatus with $KClO_4$ as the oxygen source. Comprehensive characterization combining x-ray diffraction, STEM, and high-pressure electrical resistance measurements reveals two key findings: (1) the oxygen stoichiometry in $La_3Ni_2O_{7+\delta}$ can be precisely controlled by varying the $KClO_4$ content; and (2) while the critical pressure is reduced in $La_3Ni_2O_{7.16}$, its critical temperature is lower than that of the as-grown samples.

The oxygen-annealed $La_3Ni_2O_{7+\delta}$ polycrystals were synthesized through a two-step process. First, the parent $La_3Ni_2O_{7-\delta}$ sample was prepared using the sol–gel method according to established protocols,[47] referred to as the as-grown sample. For the oxygen annealing step, the as-grown sample was thoroughly ground with $KClO_4$ as an oxygen donor in three distinct molar ratios of $KClO_4$:$La_3Ni_2O_{7+\delta}$ = 0.08:1 for sample S1, 0.2:1 for S2, and 1:1 for sample S3. The homogeneous mixtures were then pressed into pellets and subjected to high-pressure annealing in a piston-cylinder-type high-pressure apparatus under precisely controlled conditions of 973 K and 2 GPa for 1 hour. To minimize the influence of KCl, following the annealing process, the resulting products were carefully reground and washed with deionized water to remove residual KCl byproduct. After each wash, the mixture was centrifuged to separate the solid from the water. The final oxygen-annealed samples were denoted as S1, S2, and S3.

The crystal structure was determined by room-temperature powder x-ray diffraction (XRD) using a PANalytical x-ray diffractometer with Cu-$K\alpha$ radiation. Rietveld refinement of the XRD patterns was conducted using the GSAS software package. Thermogravimetric analysis (TGA) was done by NETZSCH STA 449 F3, using 10% H_2/Ar flow at a rate of 150 mL/min, and the maximum temperature was 800 °C with heating rate 7.5 °C/min. The HAADF-STEM images were acquired on a Thermo Fisher Scientific Themis *Z* microscope working at 300 kV. Electrical resistance measurements under high pressure were carried out with a screw-pressure-type diamond anvil cell (DAC) made of non-magnetic Be–Cu alloy. The diamond with 500 μm culet was used to provide pressure within 50 GPa. The steel gasket was utilized, and a hole with the size of 200 μm is predrilled as the sample holder. The electrodes were fabricated from 5 μm-thick Pt foil. A mixture of epoxy and cubic BN was used as insulating layer between gasket and electrodes. High-purity KBr (5N) served as pressure transmitting medium (PTM). The pressure was characterized by the shift of ruby fluorescence at room temperature. Electrical resistance was collected on a Quantum Design physical properties measurement system (PPMS DynaCool). Standard four-probe method was used for electrical resistance measurements at ambient pressure, and the Van-der-Pauw method was adopted for measurements at high pressure.

Figure 1(a) presents the powder XRD patterns of as-grown $La_3Ni_2O_{7-\delta}$ and the oxygen-annealed polycrystals (S1, S2, and S3). The XRD pattern of the as-grown sample is well refined with the orthorhombic phase, and the patterns of S1, S2 and S3 were successfully refined using a two-phase model consisting of the orthorhombic phase (space group *Amam*, No. 63) and the tetragonal phase (space group *I*4/*mmm*, No. 139). The refinement results are summarized in Table 1. For S1 and S2, the lattice parameters of the orthorhombic phase show minimal deviation ($< 0.1\%$) from those of the as-grown $La_3Ni_2O_{7-\delta}$.[47] In contrast, S3 exhibits a 0.25% contraction along the *c*-axis while maintaining comparable in-plane parameters to the as-grown sample. The *c*-axis contraction, previously observed in high-oxygen-pressure annealed $La_3Ni_2O_{7+\delta}$ and $La_2PrNi_2O_{7+\delta}$ polycrystals,[45,46] likely originates from enhanced interlayer interactions induced by interstitial oxygen incorporation. The enlarged view of the diffraction peaks between 30° and 35° is shown in Fig. 1(b) demonstrating the shift of the diffraction peaks clearly. Such shift is consistent with the corresponding changes in the lattice parameters. We also attempted to refine the XRD pattern of S3 using the orthorhombic phase and the superstructure phase reported in Ref. [45] (see Fig. S1). However, the poor refinement

results suggest that the superstructure likely has not formed in S3. Phase quantification reveals distinct oxygen-content dependence: the orthorhombic phase fraction is 65.8 wt% in S1, 55.8 wt% in S2, and 37.6 wt% in S3, and the tetragonal phase fraction increases correspondingly. This demonstrates that high-pressure oxygen annealing using $KClO_4$ as an oxygen donor facilitates the orthorhombic-tetragonal phase transition in $La_3Ni_2O_{7+\delta}$, consistent with the behavior observed in Co-doped analogues.[47] Notably, the relative phase fractions can be precisely controlled by varying the $KClO_4$ content.

The oxygen content of the annealed samples S1, S2, and S3 was determined by thermogravimetric analysis in 10% H_2/Ar gas, and the results are shown in Fig. 1(c). The oxygen content was calculated according to the weight loss and displayed as the vertical axis in Fig. 1(c). Consistent with previous reports,[47,48] two stages are observed as temperature increases. First, a metastable phase $La_3Ni_2O_{6.45}$ is formed at $\sim$ 500 °C, and eventually La_2O_3 and elemental Ni is obtained after full reduction. The average oxygen content is estimated to be 7.16 for S1, 7.29 for S2, and 7.38 for S3, which are larger than the value 6.94 for the as-grown sample.[47] The obtained oxygen content increases with the amount of used $KClO_4$. The high-pressure annealing using solid-state $KClO_4$ as oxygen source presents several advantages over conventional high-oxygen-pressure method. First, high pressure high temperature synthesis is a good way to stabilize metastable phases, as demonstrated in the synthesis of cuprates with high oxygen content. Second, it enables precise and continuous tuning of the oxygen atmosphere by simply varying the amount of $KClO_4$ in the mixture. Third, the intimate mixture of $KClO_4$ with precursor ensures a localized and uniform oxidizing environment at the reaction interface, thereby promoting homogeneous reaction. The large value of 7.38 for S3 can be attributed to the interstitial oxygen, and the coexistence of multilayer nickelates, as discussed below.

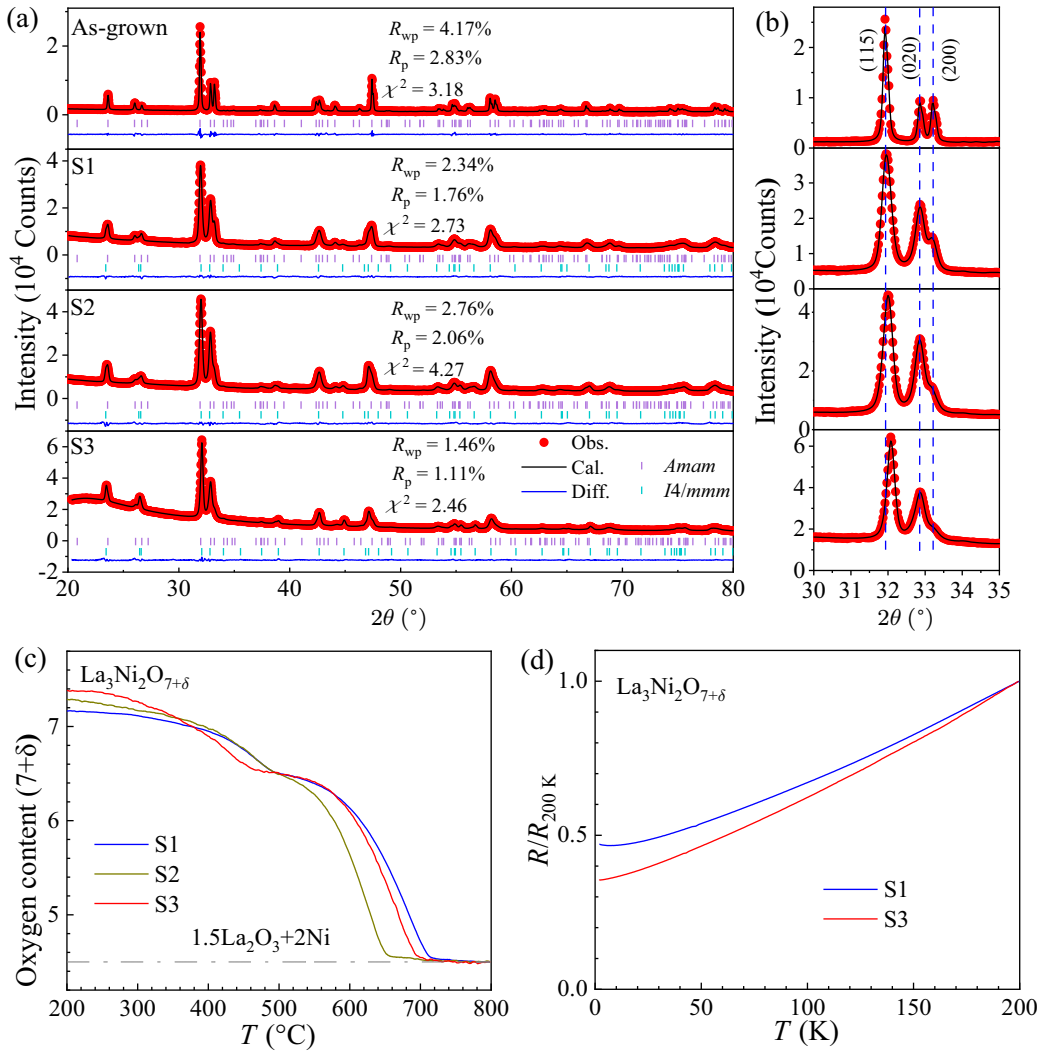


Fig. 1. (a) The Rietveld refinement of XRD patterns of the as-grown polycrystals and the oxygen-annealed samples denoted as S1, S2, and S3. The fit parameters are shown in inset. (b) The enlarged view of (a) in the range of 30°–35°. The vertical dashed lines mark the diffraction peaks of the orthorhombic phase in the as-grown sample. (c) The thermogravimetric curves for the oxygen-annealed $La_3Ni_2O_{7+\delta}$ polycrystals. The oxygen content was calculated with the weight percent loss and shown as the vertical axis. The average oxygen content is estimated to be 7.16 (S1), 7.29 (S2), and 7.38 (S3). (d) The temperature dependence of normalized resistance of S1 and S3, which shows metallic behavior.

Table 1. The lattice parameters from refinements and the oxygen-content from TGA analysis of each phase for the as-grown sample, S1, S2, and S3, and the weight fraction of the orthorhombic phase.

Samples	Lattice parameters	Space: *Amam*	Space: *I*4/*mmm*	Oxygen-content	Weight fraction
S1	*a* (Å)	5.396 (9)	3.863 (9)	$La_3Ni_2O_{7.16}$	65.8%
	b (Å)	5.450 (6)	3.863 (9)		
	c (Å)	20.532 (9)	20.26 (02)		
	V (Å^3)	604.0 (05)	302.4 (80)		
S2	*a* (Å)	5.406 (8)	3.8559 (1)	$La_3Ni_2O_{7.29}$	55.8%
	b (Å)	5.458 (7)	3.8559 (1)		
	c (Å)	20.53 (26)	20.20 (80)		
	V (Å^3)	606.0 (05)	300.3 (56)		
S3	*a* (Å)	5.395 (7)	3.8573 (6)	$La_3Ni_2O_{7.38}$	37.6%
	b (Å)	5.449 (3)	3.8573 (6)		
	c (Å)	20.47 (63)	20.186 (3)		
	V (Å^3)	602.0 (67)	300.3 (56)		
As-grown	*a* (Å)	5.392 (4)		$La_3Ni_2O_{6.94}$	100%
	b (Å)	5.448 (2)			
	c (Å)	20.532 (9)			
	V (Å^3)	603.2 (33)			

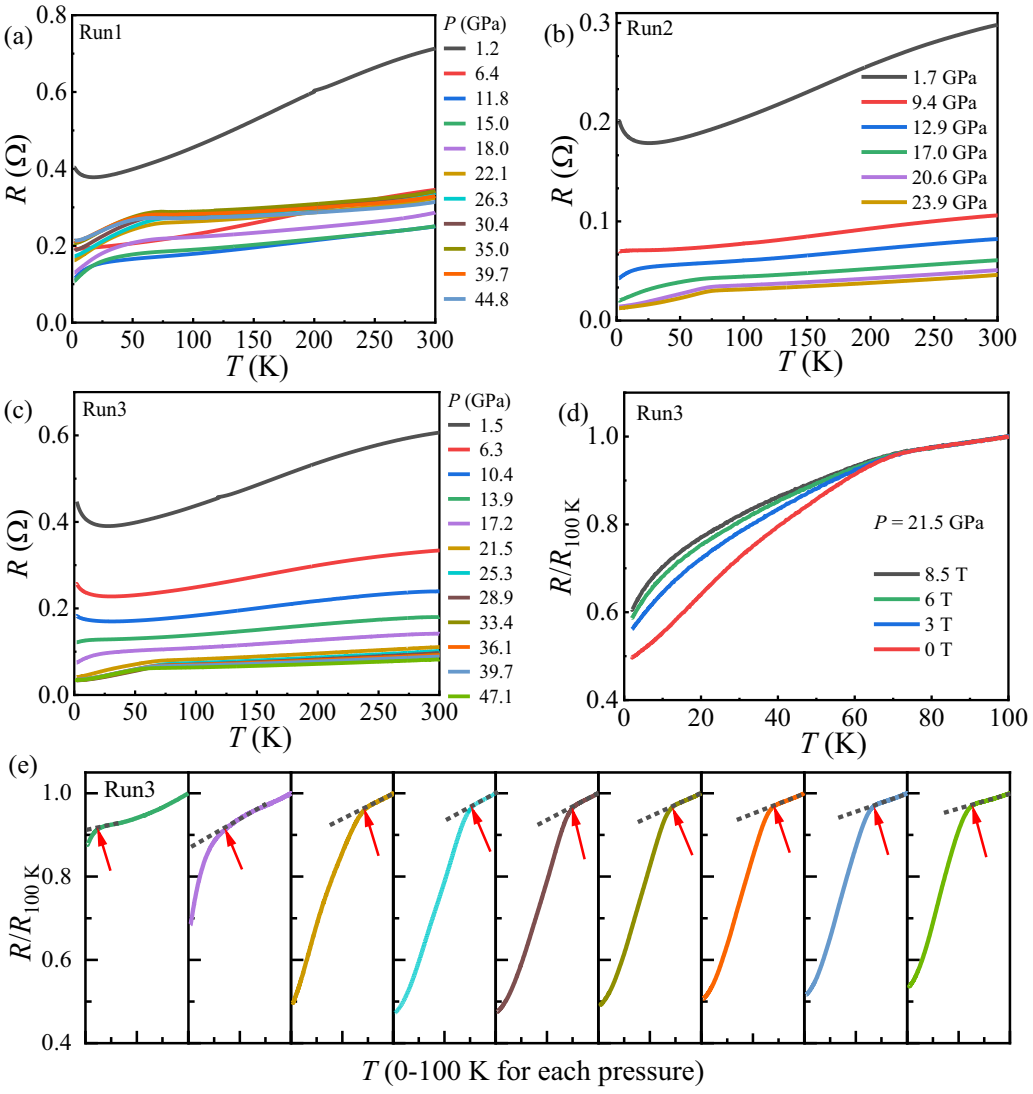


Fig. 2. (a)–(c) The temperature dependence of resistance at various pressures of three samples for $La_3Ni_2O_{7.16}$ which are denoted as Run1, Run2, and Run3. (d) The superconductivity under various magnetic fields at 21.5 GPa for Run3. (e) The superconductivity at various pressures for Run3. The red arrows display the superconducting transition.

The temperature dependence of resistance for S1 and S3 exhibits metallic behavior, as displayed in Fig. 1(d). This is different from the recent oxygen-annealing studies at high oxygen pressure, in which the resistance curves show semiconductor-like upturn behavior at low temperature and an evidenced DW anomaly.[44,45] The metallic behavior is also observed in the samples with oxygen content approaching to 7 reported in early studies.[48,49]

The electrical resistance measurements on the oxygen-annealed $La_3Ni_2O_{7+\delta}$ polycrystals $La_3Ni_2O_{7.16}$ and $La_3Ni_2O_{7.38}$ under high pressures up to 47.1 GPa were carried out with nonmagnetic DAC, and the results are shown in Figs. 2 and 3. Consistent with ambient pressure data, both $La_3Ni_2O_{7.16}$ and $La_3Ni_2O_{7.38}$ show metallic behavior, while a resistance upturn behavior was observed below 25 K at low pressures, which may be due to the effect of grain boundaries since powder samples were used for the measurements. This upturn behavior has also been observed in high-pressure measurements on as-grown $La_3Ni_2O_{7-\delta}$ polycrystals.[26,28]

Three samples were used for the high-pressure electrical resistance measurements for $La_3Ni_2O_{7.16}$, which are denoted as Run1, Run2 and Run3 (Fig. 2). A slight resistance drop was observed below 10 K at 9.4 GPa in Run2 (Fig. 2(b)). The drop becomes pronounced with further compressing. The results are confirmed by other measurements Run1 and Run3 (Figs. 2(a) and 2(c)). The maximum drop of resistance reaches 52% at 25.3 GPa in Run3. Magnetic field was applied to further investigate the resistance drop, and the results are shown in Fig. 2(d). The transition temperature is insensitive to the magnetic field, and only slightly shifts to lower temperature with the increase of magnetic field. This is consistent with the magnetic field dependence of superconductivity in $La_3Ni_2O_{7-\delta}$,[26,28,33] confirming that the drop is due to superconducting transition. The transition under various pressures of Run3 is displayed in Fig. 2(e), and the transition temperature is marked by the red arrows. Upon compressing, the transition temperature increases initially, and reaches a maximum of 76 K at 25.3 GPa, followed by a decrease as pressure further increases. However, no zero resistance was achieved similar to other high-pressure measurements on polycrystals with DAC method.[26,28,30]

High pressure electrical resistance measurements were carried out on two samples for $La_3Ni_2O_{7.38}$ which are represented by Run1 and Run2. Distinct from large resistance drop in $La_3Ni_2O_{7.16}$, a weak drop was detected in $La_3Ni_2O_{7.38}$ as shown in Figs. 3(a) and 3(c). The resistance drop first emerged at 19.6 GPa with a T_c of 74 K in Run1. Two small drops appeared in Run2 (Fig. 3(d)). The lower-temperature one starts at 16.9 GPa. The transition temperature initially increases, and then almost stabilizes, persisting up to 45.3 GPa, with a maximum of about 20 K. The higher-temperature drop is similar to that in Run1, in which a tiny drop shows up at around 20 GPa, and the highest transition temperature is about 76 K. The feature of the resistance drops is reminiscent of the superconductivity in $La_4Ni_3O_{10-\delta}$ and $La_3Ni_2O_{7-\delta}$ polycrystals.[22,23,26,28,33] The higher-temperature transition corresponds to the superconducting transition of bilayer nickelate polycrystals, and the lower-temperature transition is attributed to trilayer nickelate polycrystals. The observation of superconducting signature with oxygen content of 7.16 or 7.38 is consistent with the oxygen-content range obtained by electrochemical method.[35]

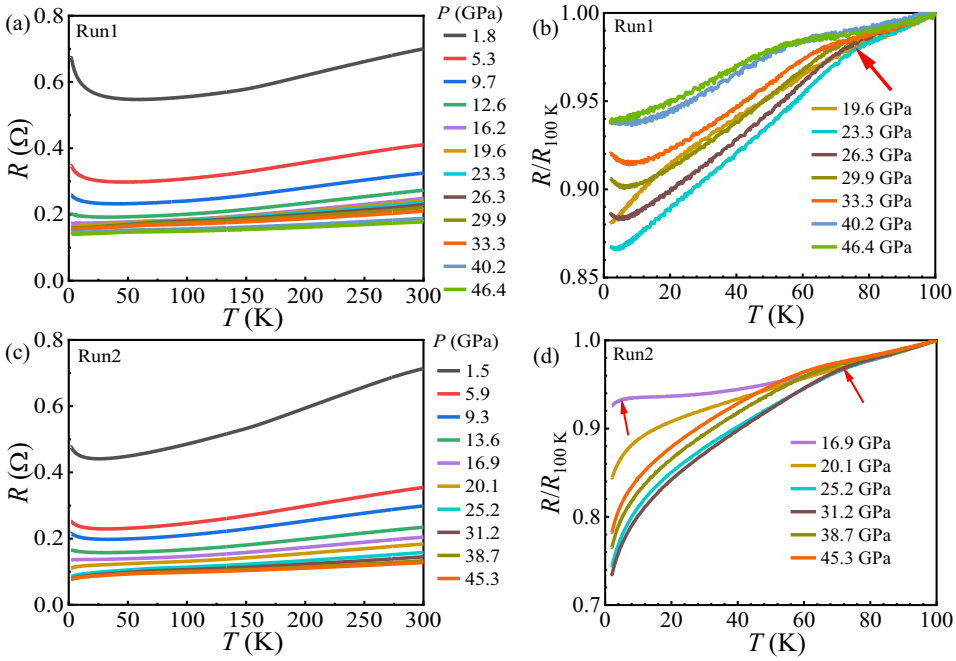


Fig. 3. (a) and (c) The temperature dependence of electrical resistance at various pressures of two samples for $La_3Ni_2O_{7.38}$ denoted as Run1 and Run2. (b) and (d) The superconductivity at various pressures for Run1 and Run2.

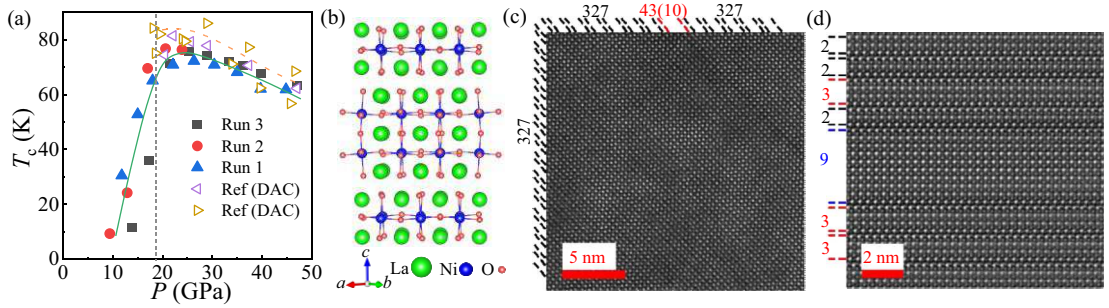


Fig. 4. (a) The pressure dependence of superconducting T_c for $La_3Ni_2O_{7+\delta}$ polycrystal $La_3Ni_2O_{7.16}$, and we also include the T_c of as-grown $La_3Ni_2O_{7-\delta}$ polycrystals from Refs. [26,28]. The short-dash line and the solid line are guides for the eye. The short vertical dot line marks the critical pressure for as-grown sample measured with DAC method. (b) The schematic structure of $La_3Ni_2O_7$ crystal structure in [110] view. (c) and (d) The typical atomicscale HAADF-STEM images along [110] orientation for $La_3Ni_2O_{7.16}$ and $La_3Ni_2O_{7.38}$. The notation 327 and 2 indicate the bilayer phase $La_3Ni_2O_7$, 43(10) and 3 denote the trilayer phase $La_4Ni_3O_{10}$, while 9 refers to $La_{10}Ni_9O_{28}$ which contains 9 layers of Ni–O planes.

The crystal quality of $La_3Ni_2O_{7.38}$ is poor as discussed below, and the signature of superconducting transition is tiny. Here, only the superconducting T_c of $La_3Ni_2O_{7.16}$ was summarized in Fig. 4(a). To elucidate the effect of oxygen-annealing on the superconductivity of $La_3Ni_2O_7$, the T_c of as-grown $La_3Ni_2O_{7-\delta}$ polycrystals obtained by DAC method from Ref. [28], and Ref. [26] was also included in the diagram. The samples measured in the references show upturn behavior at low temperature and a DW transition at $\sim$ 140 K. In contrast, $La_3Ni_2O_{7.16}$ exhibits metallic behavior, which implies that the oxygen content in the annealed sample is higher. Figure 4(a) demonstrates that superconducting T_c of $La_3Ni_2O_{7.16}$ is lower than the value from references, suggesting that the T_c is lower along with higher oxygen content. This has also been observed in $La_{3-x}Sr_xNi_2O_{7-\delta}$ thin films correlated with the variation of carrier density.[50] The critical pressure (P_c) varies slightly among these samples, and the value is in the vicinity of 11 GPa. Notably, this is substantially lower than the approximate 20 GPa typically required for as-grown polycrystalline samples. High-pressure studies on polycrystals with $\delta = 0$ and 0.12 also reveal the slight decrease of T_c for 0.12. However, the critical pressure is significantly large for both samples (approximately 25 GPa).[51] The resistance drop here is larger, reaching 52%. Note that $La_3Ni_2O_{7.16}$ only contains 65.8 wt% orthorhombic phase, while it shows better signature of superconductivity compared with the as-grown samples.[26,28] Thus, the orthorhombic phase with lower oxygen vacancies likely favors bulk superconductivity with reduced critical pressure. However, as oxygen content further increases, the signature of superconductivity becomes pretty weak in $La_3Ni_2O_{7.38}$.

The as-grown $La_3Ni_2O_{7-\delta}$ polycrystals show ubiquitous intergrowth of 327 with 4310 and 214 phases, and great inhomogeneity in oxygen vacancies,[38,44,46] which may destroy the superconductivity. Here, we carried out STEM measurements on $La_3Ni_2O_{7.16}$ and $La_3Ni_2O_{7.38}$, and the typical atomic-scale HAADF-STEM images along [110] orientation are displayed in Figs. 4(c) and 4(d). More STEM images are shown in Fig. S2 in the supplemental materials. The bilayer phase is denoted as 327 or simply 2. The numbers 3 and 9 represent the phases with 3- and 9-layer of Ni–O planes per unit. $La_3Ni_2O_{7.16}$ consists of large-area stacking of bilayer phase (Figs. 4(c) and S2(a)–S2(d)), the structure of which is displayed in Fig. 4(b). It intergrows with a few La_2NiO_4 or $La_4Ni_3O_{10}$ layer, similar to $La_2PrNi_2O_7$.[27] Using more $KClO_4$ in $La_3Ni_2O_{7.38}$ results in the intergrowth with other R–P compounds containing more layers of Ni–O plane (Figs. 4(d), S2(e) and S2(f)). The observation of large area of $La_4Ni_3O_{10}$ in $La_3Ni_2O_{7.38}$ is consistent with the detection of the superconducting signature of $La_4Ni_3O_{10}$.

Regarding the superconductivity of $La_3Ni_2O_{7+\delta}$, $La_3Ni_2O_{7.16}$ demonstrates better superconducting transition with low critical pressure and good signature of superconductivity, while only tiny signal was detected in $La_3Ni_2O_{7.38}$. Several reasons may lead to these distinct differences. First, the noticeable intergrowth of other R–P phases in $La_3Ni_2O_{7.38}$ may destroy superconductivity. Second, according to the XRD analysis, $La_3Ni_2O_{7.16}$ is a mixture of 65.8 wt% orthorhombic phase and 34.2% tetragonal phase, while $La_3Ni_2O_{7.38}$ consists of 37.6 wt% orthorhombic phase and 62.4 wt% tetragonal phase. The tetragonal phase may do not support superconductivity, which is in agreement with previous report that tetragonal phase shows no superconductivity up to 70 GPa.[52] Third, the interstitial oxygen may destroy the superconductivity in $La_3Ni_2O_{7.38}$. The c lattice in $La_3Ni_2O_{7.38}$ contracts obviously while the c lattice of $La_3Ni_2O_{7.16}$ is close to that of the as-grown $La_3Ni_2O_{7-\delta}$ according to the above analysis of XRD patterns. This may imply that unignorable interstitial oxygen appears in $La_3Ni_2O_{7.38}$ similar to the oxygen-annealed $La_3Ni_2O_{7+\delta}$ and $La_2PrNi_2O_{7+\delta}$ polycrystals, in which the interstitial oxygen suppresses the superconductivity.[45,46] Our studies suggest that proper oxygen annealing, which eliminates the oxygen deficiencies and acts as a hole-doping mechanism, reduces the critical pressure while concurrently lowers the T_c. Electron doping implemented by ensuring low deficiencies may provide a viable way to achieve bulk superconductivity with an enhanced T_c in $La_3Ni_2O_7$.

In summary, we performed controlled oxygen annealing of $La_3Ni_2O_{7+\delta}$ polycrystals using a piston-cylinder-type high-pressure apparatus with $KClO_4$ as the oxygen source. This approach successfully yielded high-oxygen-content samples (S1: $La_3Ni_2O_{7.16}$; S2: $La_3Ni_2O_{7.29}$; S3: $La_3Ni_2O_{7.38}$) as confirmed by TGA. S1 and S3 exhibited metallic behavior at ambient pressure. Microstructural characterization revealed distinct phase behaviors: STEM showed that S1 maintains large-area bilayer $La_3Ni_2O_7$ phase purity, while S3 displays significant intergrowth with other R–P phases. XRD quantification indicated S3 contains only 37.6 wt% orthorhombic phase, with a 0.25% shrinkage in the *c*-lattice parameter suggesting interstitial oxygen incorporation. High-pressure electrical resistance measurements demonstrated contrasting superconducting responses: S1 showed lower critical pressure and good superconducting signature albeit with reduced T_c compared to as-grown samples, whereas S3 exhibited only marginal superconductivity. The results establish that $KClO_4$-assisted high-pressure synthesis provides an effective route for oxygen stoichiometry control in $La_3Ni_2O_{7+\delta}$, offering new opportunities for optimizing nickelate superconductivity through targeted oxygen content engineering.

Acknowledgments

Project supported by the National Key R&D Program of China (Grant No. 2022YFA1403203), the National Natural Science Foundation of China (Grant Nos. 12204007, 12374133, 12304162, and 12074002), the Key Scientific Research Foundation of the Education Department of Anhui Province (Grant No. 2024AH050046), the Innovation Program for Quantum Science and Technology (Grant No. 2021ZD0302802), Quantum Science and Technology-National Science and Technology Major Project (Grant No. 2024ZD0301300), the Major Basic Program of Natural Science Foundation of Shandong Province (Grant No. ZR2021ZD01), the Start-up Funding Program of Guangdong–Hong Kong–Macao Greater Bay Area Quantum Science Center (Grant No. QD2301003), and Guangdong Provincial Quantum Science Strategic Initiative (Grant No. GDZX2401001).

References

[1] Bednorz J G and Müller K A 1986 *Z. Phys. B Condens. Matter* **64** 189
[2] Wu M K, Ashburn J R, Torng C J, Hor P H, Meng R L, Gao L, Huang Z J, Wang Y Q and Chu C W 1987 *Phys. Rev. Lett.* **58** 908
[3] Zhao Z X, Chen L Q, Yang Q S, Huang Y Z, Chen G H, Tang R M, Liu G R, Cui C G, Chen L, Wang L Z, Guo S Q, Li S L and Bi J Q 1987 *Chin. Sci. Bull.* **32** 412
[4] Lee P A, Nagaosa N and Wen X G 2006 *Rev. Mod. Phys.* **78** 17
[5] Johnston D C 2010 *Adv. Phys.* **59** 803
[6] Sun H, Huo M, Hu X, Li J, Liu Z, Han Y, Tang L, Mao Z, Yang P, Wang B, Cheng J, Yao D X, Zhang G M and Wang M 2023 *Nature* **621** 493
[7] Liu Y B, Mei J W, Ye F, Chen W Q and Yang F 2023 *Phys. Rev. Lett.* **131** 236002
[8] Luo Z, Hu X, Wang M, Wu W and Yao D X 2023 *Phys. Rev. Lett.* **131** 126001
[9] Chen K, Liu X, Jiao J, Zou M, Jiang C, Li X, Luo Y, Wu Q, Zhang N, Guo Y and Shu L 2024 *Phys. Rev. Lett.* **132** 256503
[10] Chen X, Choi J, Jiang Z, Mei J, Jiang K, Li J, Agrestini S, Garcia-Fernandez M, Sun H, Huang X, Shen D, Wang M, Hu J, Lu Y, Zhou K J and Feng D 2024 *Nat. Commun.* **15** 9597
[11] Liu Z, Huo M, Li J, Li Q, Liu Y, Dai Y, Zhou X, Hao J, Lu Y, Wang M and Wen H H 2024 *Nat. Commun.* **15** 7570
[12] Meng Y, Yang Y, Sun H, Zhang S, Luo J, Chen L, Ma X, Wang M, Hong F, Wang X and Yu X 2024 *Nat. Commun.* **15** 10408
[13] Qu X Z, Qu D W, Chen J, Wu C, Yang F, Li W and Su G 2024 *Phys. Rev. Lett.* **132** 036502
[14] Sakakibara H, Kitamine N, Ochi M and Kuroki K 2024 *Phys. Rev. Lett.* **132** 106002
[15] Wang M, Wen H H, Wu T, Yao D X and Xiang T 2024 *Chin. Phys. Lett.* **41** 077402
[16] Xie T, Huo M, Ni X, Shen F, Huang X, Sun H, Walker H C, Adroja D, Yu D, Shen B, He L, Cao K and Wang M 2024 *Sci. Bull.* **69** 3221
[17] Yang J, Sun H, Hu X, Xie Y, Miao T, Luo H, Chen H, Liang B, Zhu W, Qu G, Chen C Q, Huo M, Huang Y, Zhang S, Zhang F, Yang F, Wang Z, Peng Q, Mao H, Liu G, Xu Z, Qian T, Yao D X, Wang M, Zhao L and Zhou X J 2024 *Nat. Commun.* **15** 4373
[18] Zhang Y, Lin L F, Moreo A, Maier T A and Dagotto E 2024 *Nat. Commun.* **15** 2470
[19] Wang Y, Jiang K, Ying J, Wu T, Cheng J, Hu J and Chen X 2025 *Natl. Sci. Rev.* **12** nwaf373
[20] Wang Z, Zhang H J, Jiang K and Zhang F C 2025 *Natl. Sci. Rev.* **12** nwaf353
[21] Li Q, Zhang Y J, Xiang Z N, Zhang Y, Zhu X and Wen H H 2024 *Chin. Phys. Lett.* **41** 017401
[22] Zhu Y, Peng D, Zhang E, Pan B, Chen X, Chen L, Ren H, Liu F, Hao Y, Li N, Xing Z, Lan F, Han J, Wang J, Jia D, Wo H, Gu Y, Gu Y, Ji L, Wang W, Gou H, Shen Y, Ying T, Chen X, Yang W, Cao H, Zheng C, Zeng Q, Guo J G, Zhao J 2024 *Nature* **631** 531
[23] Zhang E, Peng D, Zhu Y, Chen L, Cui B, Wang X, Wang W, Zeng Q and Zhao J 2025 *Phys. Rev. X* **15** 021008
[24] Huang C, Li J, Huang X, Zhang H, Hu D, Huo M, Chen X, Chen Z, Sun H and Wang M 2025 arXiv:2510.12250 [cond-mat.supr-con]
[25] Shi M, Peng D, Fan K, Xing Z, Yang S, Wang Y, Li H, Wu R, Du M, Ge B, Zeng Z, Zeng Q, Ying J, Wu T and Chen X 2025 *Nat. Phys.* **21** 1780
[26] Feng J J, Han T, Song J P, Long M S, Hou X Y, Zhang C J, Mu Q G and Shan L 2024 *Phys. Rev. B* 110 L100507
[27] Wang N, Wang G, Shen X, Hou J, Luo J, Ma X, Yang H, Shi L, Dou J, Feng J, Yang J, Shi Y, Ren Z, Ma H, Yang P, Liu Z, Liu Y, Zhang H, Dong X, Wang Y, Jiang K, Hu J, Nagasaki S, Kitagawa K, Calder S, Yan J, Sun J, Wang B, Zhou R, Uwatoko Y and Cheng J 2024 *Nature* **634** 579
[28] Zhang M, Pei C, Wang Q, Zhao Y, Li C, Cao W, Zhu S, Wu J and Qi Y 2024 *J. Mater. Sci. Technol.* **185** 147
[29] Li F, Xing Z, Peng D, Dou J, Guo N, Ma L, Zhang Y, Wang L, Luo J, Yang J, Zhang J, Chang T, Chen Y S, Cai W, Cheng J, Wang Y, Liu Y, Luo T, Hirao N, Matsuoka T, Kadobayashi H, Zeng Z, Zheng Q, Zhou R, Zeng Q, Tao X and Zhang J 2026 *Nature* **649** 871
[30] Qiu Z, Chen J, Semenok D V, Zhong Q, Zhou D, Li J, Ma P, Huang X, Huo M, Xie T, Chen X, Mao H K, Struzhkin V, Sun H and Wang M 2025 arXiv:2510.12359 [cond-mat.supr-con]
[31] Zhong Q, Chen J, Qiu Z, Li J, Huang X, Ma P, Huo M, Dong H, Sun H and Wang M 2025 arXiv:2510.13342 [cond-mat.supr-con]
[32] Hou J, Yang P T, Liu Z Y, Li J Y, Shan P F, Ma L, Wang G, Wang N N, Guo H Z, Sun J P, Uwatoko Y, Wang M, Zhang G M, Wang B S and Cheng J G 2023 *Chin. Phys. Lett.* **40** 117302
[33] Wang G, Wang N N, Shen X L, Hou J, Ma L, Shi L F, Ren Z A, Gu Y D, Ma H M, Yang P T, Liu Z Y, Guo H Z, Sun J P, Zhang G M, Calder S, Yan J Q, Wang B S, Uwatoko Y and Cheng J G 2024 *Phys. Rev. X* **14** 011040
[34] Li J, Peng D, Ma P, Zhang H, Xing Z, Huang X, Huang C, Huo M, Hu D, Dong Z, Chen X, Xie T, Dong H, Sun H, Zeng Q, Mao H K and Wang M 2025 *Natl. Sci. Rev.* **12** nwaf220
[35] Zhou Y, Guo J, Cai S, Sun H, Li C, Zhao J, Wang P, Han J, Chen X, Chen Y, Wu Q, Ding Y, Xiang T, Mao H K and Sun L 2025 *Matter Radiat. Extrem.* **10** 0247684
[36] Meng W 2023 *Physics* **52** 663

[37] Wen J, Xu Y, Wang G, He Z X, Chen Y, Wang N, Lu T, Ma X, Jin F, Chen L, Liu M, Fan J W, Liu X, Pan X Y, Liu G Q, Cheng J and Yu X 2025 *Natl. Sci. Rev.* **12** nwaf268
[38] Dong Z, Huo M, Li J, Li J, Li P, Sun H, Gu L, Lu Y, Wang M, Wang Y and Chen Z 2024 *Nature* **630** 847
[39] Ko E K, Yu Y, Liu Y, Bhatt L, Li J, Thampy V, Kuo C T, Wang B Y, Lee Y, Lee K, Lee J S, Goodge B H, Muller D A and Hwang H Y 2024 *Nature* **638** 935
[40] Liu Y, Ko E K, Tarn Y, Bhatt L, Li J, Thampy V, Goodge B H, Muller D A, Raghu S, Yu Y and Hwang H Y 2025 *Nat. Mater.* **24** 1221
[41] Zhou G, Lv W, Wang H, Nie Z, Chen Y, Li Y, Huang H, Chen W, Sun Y, Xue Q K and Chen Z 2025 *Nature* **640** 641
[42] Lv W, Nie Z, Wang H, Huang H, Xue Q K, Zhou G and Chen Z 2025 *Acta Phys. Sin.* **74** 227403 (in Chinese)
[43] Hao B, Wang M, Sun W, Yang Y, Mao Z, Yan S, Sun H, Zhang H, Han L, Gu Z, Zhou J, Ji D and Nie Y 2025 *Nat. Mater.* **24** 1756
[44] Zhang Y, Pei C, Guo N, Fan L, Zhang M, Wang L, Zhang G, Li F, Wang Y, Ma C, Cheng W, Wang S, Zheng Q, Qi Y and Zhang J 2026 *J. Solid State Chem.* **355** 125757
[45] Chen X, Wang N, Zhang Q, Wang B, Wang G, Wang B, Cheng J and Gu L 2025 *Adv. Mater.* **37** e04238
[46] Dong Z, Wang G, Wang N, Dong W H, Gu L, Xu Y, Cheng J, Chen Z and Wang Y 2025 *Nat. Mater.* **24** 1927
[47] Liu Q, Yi J, Gu Y, Shi Y, Zhou M, Yuan J, He H, Chen L, Chen G, Yu J and Ren Z 2025 *J. Solid State Chem.* **351** 125528
[48] Zhang Z, Greenblatt M and Goodenough J B 1994 *J. Solid State Chem.* **108** 402
[49] Taniguchi S, Nishikawa T, Yasui Y, Kobayashi Y, Takeda J, Shamoto S and Sato M 1995 *J. Phys. Soc. Jpn.* **64** 1644
[50] Wang M, Hao B, Sun W, Yan S, Sun S, Zhang H, Gu Z and Nie Y 2026 *Phys. Rev. Lett.* **136** 066002
[51] Ueki Y, Sakurai H, Nagata H, Yamane K, Matsumoto R, Terashima K, Hirose K, Ohta H, Kato M and Takano Y 2025 *J. Phys. Soc. Jpn.* **94** 013703
[52] Shi M, Peng D, Li Y, Yang S, Xing Z, Wang Y, Fan K, Li H, Wu R, Ge B, Zeng Z, Zeng Q, Ying J, Wu T and Chen X 2025 *Nat. Commun.* **16** 9141